

Contents lists available at ScienceDirect

Materialia

journal homepage: www.elsevier.com/locate/mtla



Full Length Article

Thermally activated microstructural evolution of sputtered nanostructured Mo–Au



Joel A. Bahena^a, J. Sebastian Riano^b, Mohammed R. Chellali^c, Torben Boll^{d,e}, Andrea M. Hodge^{a,b,*}

- ^a Department of Aerospace and Mechanical Engineering, University of Southern California, 854 Downey Way, Los Angeles, CA 90089, USA
- b Department of Chemical Engineering and Materials Science, University of Southern California, 3650 McClintock Ave., Los Angeles, CA 90089, USA
- c Institute of Nanotechnology, Karlsruhe Institute of Technology, Hermann-von-Helmholtz-Platz 1, 76344 Eggenstein-Leopoldshafen, Germany
- d Institute for Applied Materials, Karlsruhe Institute of Technology, Hermann-von-Helmholtz-Platz 1, 76344 Eggenstein-Leopoldshafen, Germany
- e Karlsruhe Nano Micro Facility, Karlsruhe Institute of Technology, Hermann-von-Helmholtz-Platz 1, 76344 Eggenstein-Leopoldshafen, Germany

ARTICLE INFO

Keywords: Multilayers Nanostructured metals Segregation Atom probe tomography Thermal evolution

ABSTRACT

The microstructural evolution of a sputtered Mo–Au nanometallic multilayers was investigated by annealing samples at temperatures ranging from 350 °C to 1000 °C. Differential scanning calorimetry was used as a guide to determine critical thermal events where crucial microstructural changes could occur. Complementary techniques of transmission electron microscopy and atom probe tomography revealed distinct nanostructures at the selected temperatures, which were governed by thermal processes such as recrystallization and grain growth. As the microstructure evolved with temperature, thermodynamic and kinetic stabilization mechanisms were identified, indicating that both mechanisms appear to have a role in stabilizing the microstructure. This study highlights the complex interplay within mechanisms and processes which serves as a roadmap for understanding the developments of nanoscale structures.

1. Introduction

Nanostructured materials are of considerable interest as they exhibit unique properties that are attributed to their nanoscale features. However, the high density of grain boundaries (GBs) that is intrinsic to nanostructure materials, generates a thermodynamic driving force that promotes significant grain growth [1,2]. This inherent microstructural instability has limited their potential to be used in commercial applications as their notable properties typically degrade with increasing grain size [3-6]. To counteract the lack of stability in nanomaterials, there have been several approaches to minimize grain growth at elevated temperatures, which typically involved kinetic or thermodynamic mechanisms such as Zener pinning or reducing GB energy through secondary phase GB segregation, respectively [2,7,8]. Through these kinetic and thermodynamic approaches, various binary systems such as W-Cr, W-Ti, Cu-Nb, and Cu-Ta have all achieved improved thermal stability at elevated temperatures [9-14]. For example, a W-20 at% Ti nanostructure alloy was annealed at 1100 °C for one week and retained a 20 nm grain size through solute segregation of Ti to the GBs [15]. To date, most studies have focused in isolating either kinetic or thermodynamic mechanisms as the primary driving force for thermal stability. However, it has also been shown that these two mechanisms can occur simultaneously or consecutively [9,12] and thus the intermediate steps contributing to the overall stability are still unclear. Thermal processes such as recovery, recrystallization and grain growth should also be examined in the context of thermal evolution in nanostructured systems and could clarify and define their effects within the aforementioned mechanisms [16,17].

The nanolaminate geometry of sputtered nanostructured metallic multilayers (NMMs) presents an ideal candidate to study thermal microstructural evolution. Their synthesis allows for the control of the grain size, global composition, elemental distribution, and energetic state by tuning of the deposition parameters and layer thicknesses [18]. Additionally, sputtering can minimize the high density of defects and dislocations, along with contaminants which are associated with other synthesis techniques [12,19–22]. Current thermal studies performed on NMMs have primarily focused on the breakdown of the metallic layers by examining mechanisms such as thermal grooving and layer pinch-off [23–25]. More recent work has investigated the microstructural evolution of NMMs by annealing at elevated temperatures where distinct morphologies begin to form [26,27]. A study on the thermal evolution of Cu–W annealed at temperatures ranging from 400 to 800°C revealed several microstructural transitions that led to the eventual breakdown

E-mail address: ahodge@usc.edu (A.M. Hodge).

^{*} Corresponding author at: Department of Aerospace and Mechanical Engineering, University of Southern California, 854 Downey Way, Los Angeles, CA 90089, USA.

of the layers and the formation of a microstructure consisting of W particles embedded in a Cu matrix [26]. In another study, Hf–Ti NMMs were subjected to temperatures up to $1000\,^{\circ}$ C, where key structural transformations were identified, and the system demonstrated a unique microstructural change from a NMM to an equiaxed nanocrystalline structure [18,27]. The thermal mechanisms that induce these microstructural transformations in sputtered NMMs are still not understood, thereby emphasizing the need to further explore the thermal and microstructural evolution of these nanostructured materials.

In this study, the thermal processes that govern the microstructural evolution of sputtered Mo-Au NMMs systems are investigated. Specifically, Mo-Au nanostructures are examined at annealing temperatures ranging from 350 °C to 1000 °C, while identifying key thermally activated mechanisms. Differential scanning calorimetry (DSC) is used as a guide to determine critical thermal events where crucial microstructural changes could occur. These type of scans have been used to detect phase transformation [28,29] and thermal microstructural evolution [27] in NMMs systems. The selection of the Mo-Au alloy was based on nanocrystalline thermodynamic stability maps, where Mo-Au is predicted to achieve a stable nanograin configuration through solute-stabilized grain boundaries [30,31]. Complimentary characterization techniques of transmission electron microscopy (TEM) and atom probe tomography (APT) provide a comprehensive analysis of the microstructural transitions at different length scales over the wide range of temperatures [32]. In combining these techniques with a predicted thermally stable system, the underlying processes and mechanisms that contribute to nanograin stability can be better understood.

2. Experimental

NMMs samples with alternating Au and Mo–Au layers were synthesized using DC magnetron sputtering from high purity Au (99.99%) and Mo (99.95%) targets. A dual sputtering source system allowed for the deposition of Mo and Au onto (100) silicon substrates, with sputtering powers of 300 W and 7 W for each source, respectively. During deposition, an argon working pressure of 0.8 Pa was utilized. The resulting sputtered samples had an overall thickness of $2\,\mu\text{m}$, which were measured using an AMBIOS profilometer.

The microstructural evolution of the Mo–Au NMMs were examined over an extended temperature profile through DSC scans performed with a Labsys thermal analyzer. The enthalpy change (ΔH) of the endothermic and exothermic peaks was measured over a baseline that was removed from the scans [33]. The scans were conducted on freestanding films from 20 °C to 1000 °C at a rate of 10 °C/min under a constant argon flow of 40 ml/min. Individual pieces of the free-standing films were heat treated in a GSL1100X tube furnace (MTI Corporation) at temperatures of 350 °C, 550 °C, 800 °C, and 1000 °C for 96 h under a vacuum pressure of 5×10^{-4} Pa. Upon completion of the heat treatment, the samples were quenched in a low vapor pressure oil, (Invoil 705, Inland Vacuum Industries). A vertical tube furnace geometry was utilized that maintained quench oil temperatures near 25 °C and allowed for quenching under vacuum conditions. As a final step, samples were cleaned with ethanol after the heat-treatment process.

The microstructure and elemental compositions of the heat-treated samples were characterized by TEM and STEM using a JEOL JEM-2100F microscope combined with an EDS detector. TEM and APT lamellae of the films were prepared by Focused Ion Beam (FIB) liftouts using a JEOL FIB-4500 microscope. A 150 nm platinum protective layer was deposited onto the region of interest to minimize FIB Ga beam damage. Furthermore, APT tip preparation was performed with a ZEISS Auriga 60 FIB, resulting in needle shaped specimens with end diameters less than 100 nm. APT measurements were carried out on a CAMECA-LEAP 4000X HR instrument utilizing a laser pulsing mode with a wavelength of 355 nm. The APT parameters for samples annealed at 550 °C and 800 °C were set to a pulse energy of 100 pJ, pulse repetition rate of 100 kHz, and pulse evaporation rates of 0.3% at a base temperature of

 $60\,\mathrm{K}$. For the measurements of the $350\,^\circ\mathrm{C}$ annealed samples, the pulse energy and base temperature were decreased to $10\,\mathrm{pJ}$ and $25\,\mathrm{K}$, respectively. Reconstruction and atom probe analysis was evaluated using the CAMECA Integrated Visualization and Analysis Software (IVAS 3.6.1). A JSM-7001 scanning electron microscope (SEM) was used to determine global composition by EDS.

3. Results and discussion

The as-sputtered Mo-Au microstructure is shown in the crosssectional bright field TEM images in Fig. 1(a). The bright regions depict the 17 nm thick Mo-Au (11 at% Au) co-sputtered layers, while the darker regions represent the 2.5 nm thick Au layers (99.95 at% Au). The composition of the overall structure, as measured through SEM/EDS, was approximately 21.3 at% Au. The accompanying dark field images in Fig 1(b). illustrate the columnar structure of the as-sputtered NMMs. Over 200 grains were examined and the average grain size was determined to be 9 nm, where the grain size distribution is presented in Fig. 1(c). Grain size was calculated using similar procedures detailed in a recent study by Riano et al. [27]. The SAED pattern in the inset of Fig. 1 shows a streaked pattern with strong Mo (110) diffraction spots indicating that the sample exhibits a (110) texture. The DSC scan of the Mo-Au system is shown in Fig. 1(d) from 20 to 1000°C. From these thermal measurements, two evident exothermic peaks were observed between 400 °C and 1000 °C, which highlight microstructural transformations in the Mo-Au sample. A peak indicating recrystallization appears between temperatures of 400 °C and 500 °C with $\Delta H_{recrystallization} = -1.7$ kJ/mol. A second exothermic peak is observed starting at 620 °C and continues until the maximum tested temperature of 1000 °C suggesting grain growth with $\Delta H_{grain-growth} = -21 \text{ kJ/mol.}$

In order to determine the thermal processes associated with the identified microstructural transformations, analysis from the DSC scans was combined with direct observation of the microstructure at select annealing temperatures. Specifically, samples were heat treated to temperatures of 350 °C, 550 °C, 800 °C, and 1000 °C to capture the microstructural transformations that encompass the recrystallization and grain growth processes. Characterization of microstructural changes such as grain size, morphology, and elemental distribution throughout the microstructural evolution of the Mo-Au sample were performed through TEM and EDS. Cross-sectional TEM micrographs, EDS maps, and grain size distribution charts of the samples at different annealing temperatures are presented in Figs. 2(a)-(d). Texture and phase changes of the microstructure were also examined as a function of the annealing temperature through normalized integrated radial intensity profiles extrapolated from SAED patterns from the bright field TEM images. The respective integrated radial intensity plots are highlighted in

Furthermore, to complement TEM characterization, APT was performed on specific heat-treated samples to further examine the microstructure and to gain chemical information at a near atomic spatial resolution. In particular, APT enables the effective study of the chemical analysis of multilayer interfaces, solute segregation behaviors, and provides prevalent insights regarding microstructural evolution [34,35]. The atom probe reconstruction and corresponding concentration profiles of selected regions are presented in Figs. 4–6 which display Mo atoms (shown in blue) and Au atoms (shown in yellow) for the 350 °C, 550 °C, and 800 °C annealed samples. A comprehensive overview of the thermal evolution of the Mo–Au nanostructure, composition, microstructural changes and active thermal mechanisms will be discussed in the next sections at each selected temperature in terms of the processes.

3.1. Multilayer degradation region, T = 350 °C

The first selected temperature for this study was 350 °C; TEM images and EDS maps (Fig. 2(a)) show a multilayer structure with no noticeable

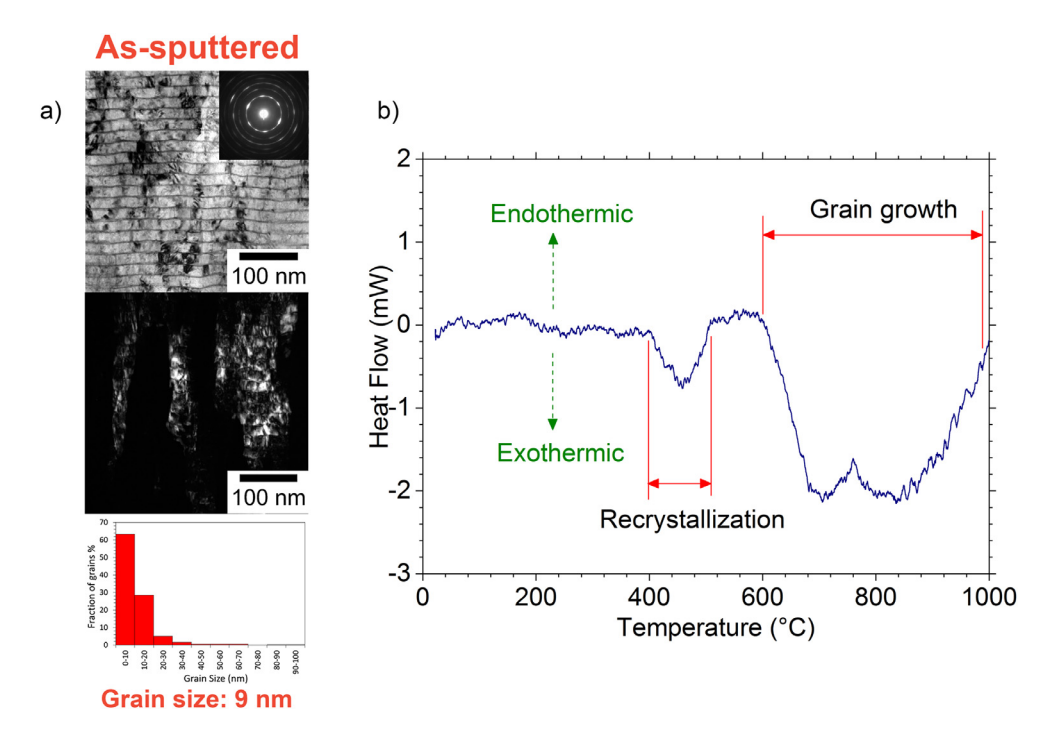


Fig. 1. Mo–Au NNMs (a) bright field TEM with inset SAED patterns (top), dark field TEM (middle), grain size distribution (bottom), and (b) differential scanning calorimetry scan of the Mo–Au multilayer from 20 °C to 1000 °C. From the scan, thermal events were indicated and enthalpy changes (Δ*H*) were calculated.

changes in the average grain size (9 nm) or grain size distribution when compared to the as-sputtered sample. At this annealing temperature, the DSC scan did not indicate any apparent thermal events. Investigation of the multilayer interface through APT compositional measurements revealed roughening and intermixing of the layers. The atom map in Fig. 4(a) reveals a multilayer structure where a 17 at% Au isosurface is applied to highlight the interfaces of the Mo-rich and Au-rich layers. Fig. 4(b) presents a 1D compositional measurement across several layers which follows the dashed arrow in Fig. 4(a). The Mo-rich layers had an average concentration of 9.1 ± 1.5 at% Au and 90.5 ± 1.6 at% Mo which matches closely to the values obtained through EDS (11 at% Au). While it is anticipated that Mo and Au should demonstrate a strong tendency to separate at this composition, the Mo-rich layers remained in a solid solution at 350 °C. Additionally, the concentration profile reveals a wide inter-diffusion region from the center of the Au-rich layers, indicating that the as-sputtered 2.5 nm Au layers have diffused and intermixed with the Mo-rich layers as a result of the increase in temperature. The centers of the Au-rich layers have an average concentration of 19.3 ± 1.9 at% Au, but the Au content gradually decreases as the measurements move further from the center. Intermixing between layers has been reported in other annealed immiscible NMMs and has been attributed to strain and interfacial contributions introduced during sputtering [36,37]. Furthermore, intermixing at the interface of the layers at increased temperatures is considered a precursor for layer breakthrough which initiates degradation of the multilayer configuration [38,39]. These findings are further supported by the SAED patterns and integrated radial intensity profiles in Figs. 2(a) and 3(b), where a decrease in the intensity of the peaks and blurring of the diffraction rings indicates a reduction in the overall crystallinity of the layered grains [40]. The streaked diffraction pattern indicates that the (110) texture of the sample was still preserved. Thus, 350 °C marks the onset of the initial stages of multilayer structure degradation in the Mo-Au system.

3.2. Recrystallization region, T = 550 °C

As the temperature is further increased to 550 °C, the microstructure of the Mo–Au NMMs undergoes significant structural and morphological changes. The original layered and columnar structure has evolved

into a nanometallic composite structure consisting of Mo-rich grains surrounded by Au solute, which is observed in the TEM micrograph and EDS map in Fig. 2(c). During this microstructural transition, the average grain size has increased to 38 nm. Similar microstructural changes have been observed in several other immiscible NMMs systems at elevated temperatures [18,23,24,26], where breakdown of the layers is generally attributed to thermal grooving, subsequent breakthrough along the columnar GBs, and eventual pinch-off of the layers [38]. Those processes are dominated by the mass transport of constituent atoms along interfaces with no significant changes in texture, suggesting that recrystallization is not associated with this morphological transformation [26,41]. However, observations of the SAED pattern (Fig. 2(b)) and the accompanying radial distribution profiles (Fig. 2(c)) reveal the loss of the streaked spot patterns and several new Mo reflections. This weakening of texture and reorientation of the grains seen in the diffraction pattern suggests a recrystallized microstructure [42,43]. Furthermore, recrystallization at this temperature, is supported by the exothermic peak seen in the DSC scan (Fig. 1(d)). Overall these findings indicate that the microstructural changes in Mo-Au at 550 °C are not fully expressed by typical multilayer degradation stages and are significantly influenced by the recrystallization process. Therefore, it is expected that recrystallization is initiated by the interfacial energy stored in the NMMs structure due to the high density of phase boundaries and strain energy generated by differences in radius between Mo and Au [44]. Thus, the stored energy drives the formations of new crystallites that consume the strained material, leading to the eventual transformation from a NMMs consisting of columnar grains to the observed nanometallic composite structure [27,45].

Similar to observations in recent NMMs studies [18,27], the segregation of the solute element appears to initiate during recrystallization, where the solute interaction with the GBs tends to dominate the thermal evolution of nanostructured materials [46,47]. Segregation of solute atoms can either enrich or form clusters and precipitates at GBs, with these behaviors contributing to limiting grain growth. To further understand solute behavior in the Mo–Au system, APT was utilized to elucidate the formation and evolution of these features along GBs in a three-dimensional space. Two APT maps were analyzed and presented

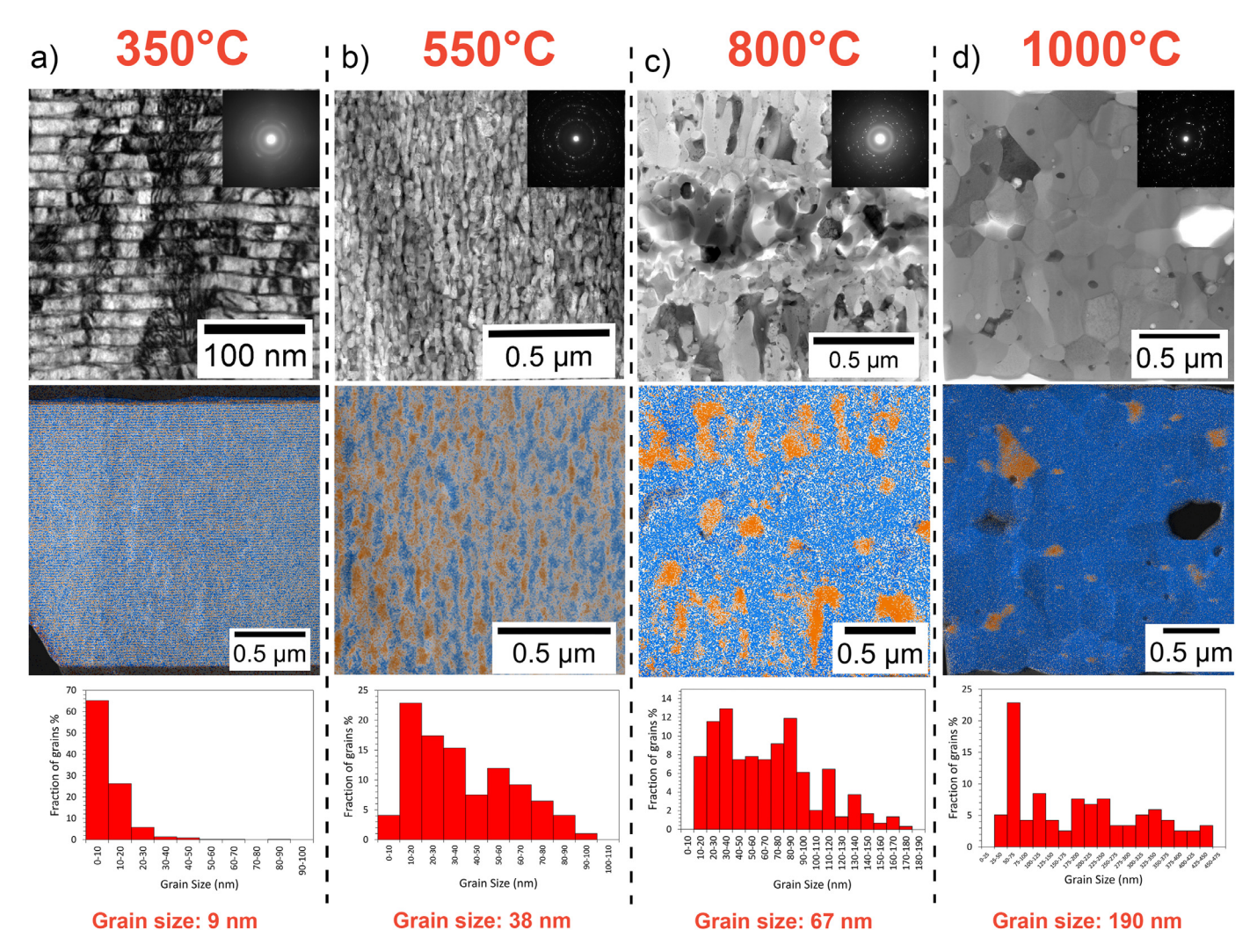


Fig. 2. Cross-sectional bright field TEM with insets of respective SAED patterns (top), corresponding EDS maps (middle), and grain size distribution (bottom) of Mo–Au samples heat-treated at (a) 350 °C, (b) 550 °C, (c) 800 °C, and (d) 1000 °C.

in Fig. 5(a.1)–(a.2). The corresponding 1D composition profiles of the regions indicated by the dashed arrows are shown in Fig. 5(b.1)–(b.2), where a distinct grain boundary is identified in each scan. Interpretation of GBs was supported by 2D chemical density plots (not shown) and the assumption that segregation species occur along 2D and 3D features [12]. A 5 at% Au isosurface was applied to the APT maps to further highlight and identify segregation zones [11,12,48] and clustering of Au solute atoms.

Analysis of the first APT map in Fig. 5(a.1), highlights a Au segregation zone that has a peak concentration of $60.8 \pm 1.4\,at\%$ Au and 38.6 ± 1.5 at% Mo, with < 1 at% O. The surrounding Mo grains reach concentrations of 97 ± 1.1 at% Mo with minimal Au content (< 1 at%), and 1 ± 0.8 at% O. The composition within the grains indicates that the Mo-Au solid solution observed in the multilayer configuration at 350 °C has decomposed after annealing to 550 °C. The detected Au segregation zone in APT correlates with the observed microstructure in the TEM and EDS maps (Fig. 2(b)) that show Au solute surrounding Morich grains. From these results, it can be inferred that as recrystallization occurs, the diffusivity near the grain boundary increases, which drives segregation of Au to the GBs resulting in GB solute enrichment and widening [15,45,49-51]. The observations are in agreement with the nanocrystalline stability maps, where the Mo-Au system was predicted to exhibit strong segregation tendencies based on the relationship between the enthalpy of segregation and enthalpy of mixing proposed by Murdoch and Schuh [31]. In addition, the segregation of Au

to the GBs is expected to minimize the driving force for grain growth by reducing the grain boundary energy, which thermodynamically stabilizes the system [46].

To further analyze the solute behavior in the Mo-Au systems at 550 °C, a second APT map of a tip extracted from a similar region is presented (Fig. 5(a.2)). In contrast to the GB shown in Fig. 5(a.1), where solute segregation of Au along GBs was exhibited, the second map (Fig 5(a.2)) revealed the presence of Au clusters along a GB. The composition through two of the clusters and the surrounding Mo-rich grains was analyzed though a 1D composition profile. The concentrations of the Au-rich clusters were measured to be ~8-9 at% Au and ~91 at% Mo with no detectable presence of contaminants. Additionally, the surrounding Mo-rich grains exhibited concentrations of 98 ± 0.5 at% Mo with traces of C and O. The formation of these solute clusters along the GBs are indicative of early onset of phase separations, which can facilitate the growth of precipitates [12,52,53]. Furthermore, solute clusters along GBs and within the matrix have been shown to reduce GB mobility in other immiscible systems [12,14,54]. Simulations of the interaction between clusters and GBs revealed stabilization mechanisms that adhere to the Zener pinning model. Specifically, a two-step interaction, with an initial attractive force accompanied by a pinning force [54]. Therefore, given the results from other studies, it is expected that the Au-rich clusters would provide a similar kinetic stabilization mechanism.

These results suggest that the Au segregation behavior along the GBs is heterogeneous, and simultaneous kinetic and thermodynamic stabi-

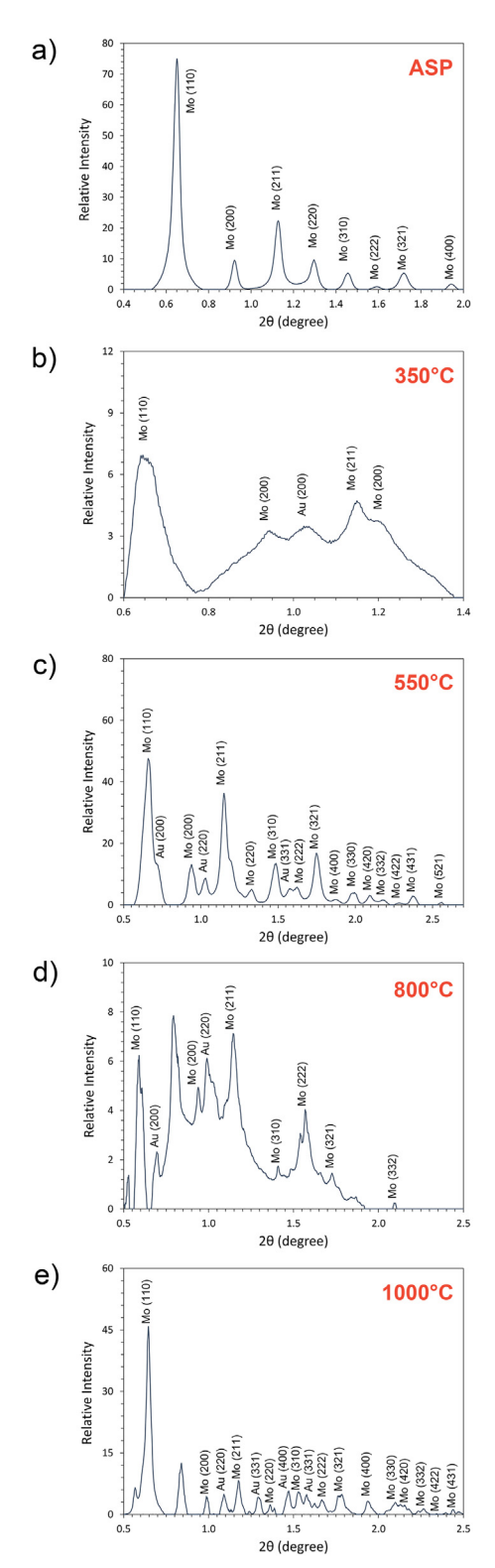


Fig. 3. Integrated radial Intensity profiles interpolated from SAED patterns obtained from Mo–Au samples (a) as-sputtered condition and heat treated at (b) $350\,^{\circ}$ C, (c) $550\,^{\circ}$ C, (d) $800\,^{\circ}$ C, and (e) $1000\,^{\circ}$ C.

lization could be occurring. The observed heterogeneous behavior of the Mo–Au systems could be dependent on several factors. Recent studies have demonstrated that immiscible alloys can exhibit different segregation tendencies depending on the GB character [53,55]. Furthermore, modeling of GB solute behavior of immiscible systems have described competing mechanisms between GB solute segregation and phase sep-

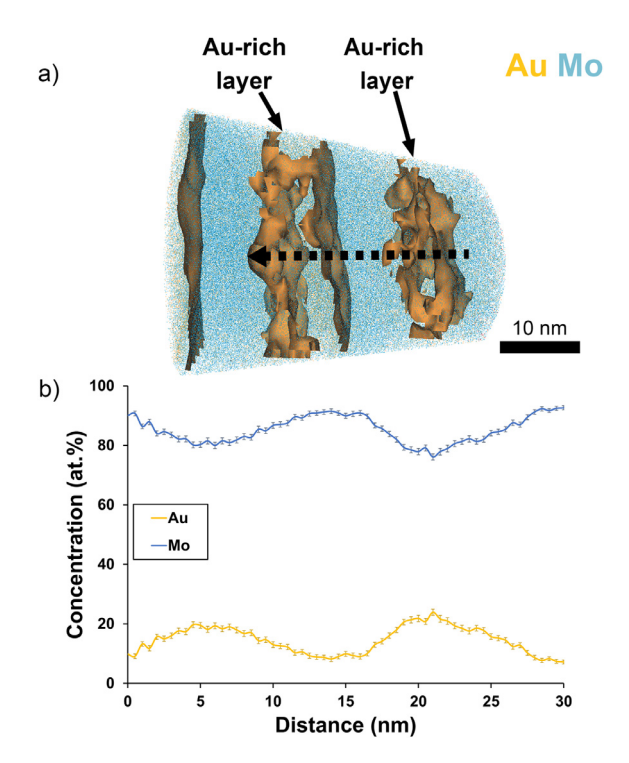


Fig. 4. (a) APT map from the Mo–Au sample annealed at $350\,^{\circ}$ C showing the multilayered structure with a $17\,$ at% Au isosurface. The 1D concentration profile (b) obtained from the region indicated by the dashed arrow shows the composition across several layers.

aration, which can lead to the observed heterogenous behavior seen in the current study [50]. Experimentally, the simultaneous occurrence of thermodynamic and kinetic stabilization mechanisms has been observed in only a few binary alloy nanostructures. For example, in Cu–Nb, Nb-enriched segregation zones and Nb-rich clusters were identified along GBs, with both kinetic and thermodynamic stability mechanisms contributing to thermal stability of the system [12]. However, the reaction of Nb clusters with oxygen impurities (~15 at% NbO and NbO₂) during synthesis complicated the ability to accurately assess solute behavior in Cu–Nb. In contrast, for the case of the Mo–Au system in this study, the APT compositional profile of the Au-enriched clusters at 550 °C show no significant concentrations of impurities indicating that these do not appear to influence the nucleation and stabilization of these clusters.

3.3. Grain growth region, $T = 800 \,^{\circ}C$

At temperatures ranging from 620 °C to 800 °C, the DSC scans indicate that grain growth should be the primary thermal process, which is in agreement with the microstructure seen at 800 °C (Fig. 2(c)). The TEM micrographs and EDS map show a similar elongated morphology to that seen at 550 °C (Fig. 2(b)), with an increase in the overall average grain size to 67 nm. In addition, the Au precipitates primarily appeared in the lower and upper portions of the film, which indicates preferential diffusion of Au solute to these regions. This behavior has also been observed in other sputtered films, for example, Ti precipitates in a Hf–Ti NMMs formed in two regions equidistance from the center of the sample when heat-treated at 1000 °C [27].

The resulting microstructure can be viewed as a transitional nanostructure that bridges the nanocomposite structure (Fig. 2(b)) to the equiaxed grain structure observed at 1000 °C (Fig. 2(d)). Specifically, when examining the microstructural evolution from 550 °C to 800 °C it is expected that the Au clusters that formed along the GBs coarsen due to increased kinetics and the high concentration of Au solute atoms present at the GBs. Furthermore, since the Mo–Au system is immiscible

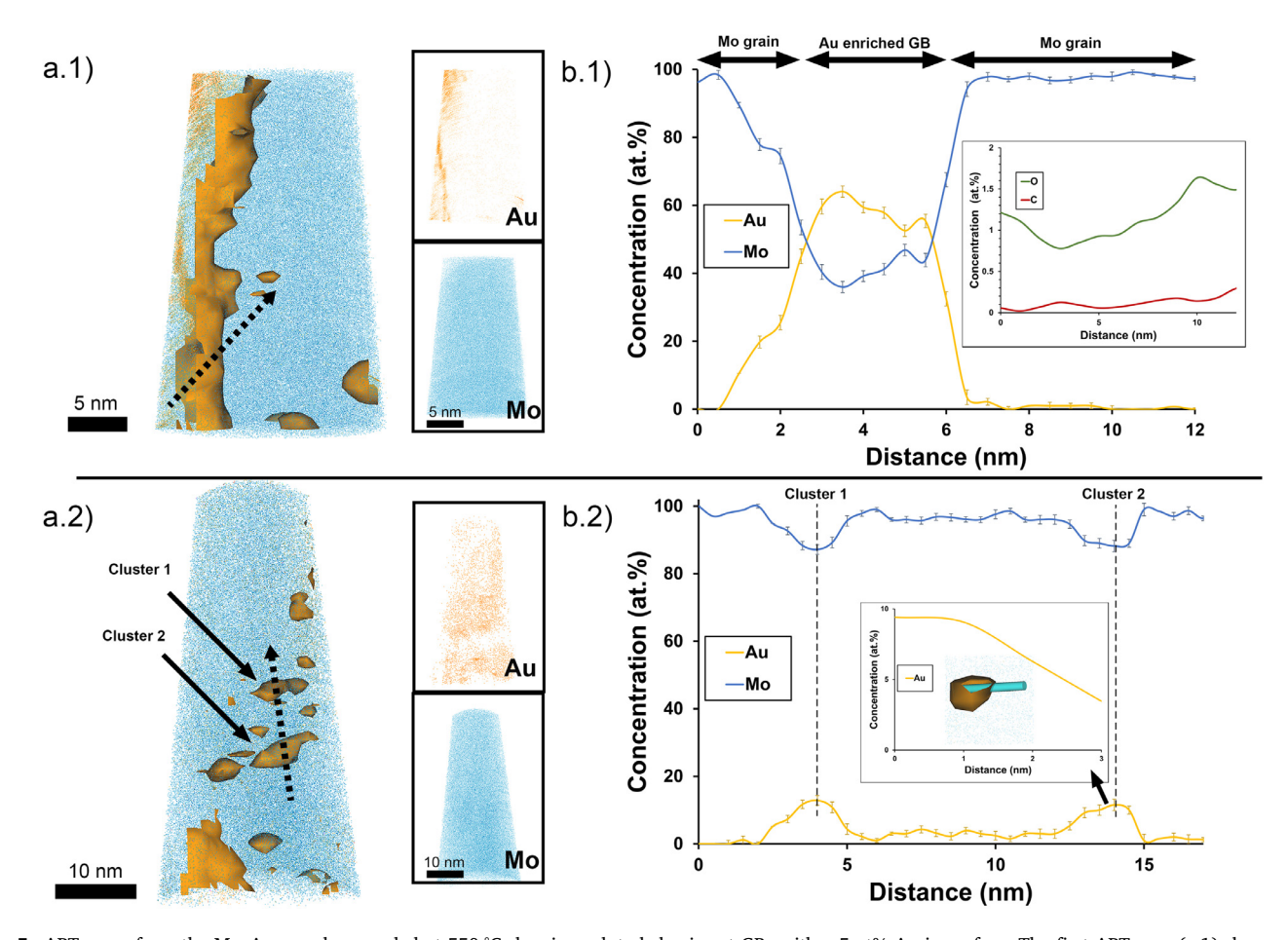


Fig. 5. APT maps from the Mo–Au sample annealed at 550 °C showing solute behavior at GBs with a 5 at% Au isosurface. The first APT map (a.1) shows an Au enriched GB (segregation zone) with insets showing individual Au and Mo ion distribution. The 1D concentration profile (b.1) is obtained through the region indicated by the dashed arrow, where the inset shows concentration of (C+O). The second APT map (a.2) shows clusters along a GB with insets showing individual Au and Mo ion distribution. The 1D concentration profile of (b.1) is obtained through the region indicated by the dashed arrow, where the inset shows the Au content through "Cluster 2" obtained from the region indicated by the blue cylinder.

and therefore thermodynamically unfavorable in a mixed configuration, sufficient heating encourages further coarsening of Au-rich precipitates until a phase separation between Mo and Au is eventually reached. The phase separation of the Mo-Au alloys was investigated through APT, where chemical analysis was performed across a Mo and Au region. The atomic distribution of the dominant elements is presented in Fig. 6(a) and (b), while Fig. 6(c) presents the 1D compositional profile through the region marked by the dashed arrow. The atom map reveals four distinct microstructural regions: two Au-rich precipitates and two Mo-rich grains. The Au and Mo regions which appear at the top and bottom, respectively, are separated from the other two grains by approximately half-spherical interfaces stemming from reconstruction problems that may be related to micro-fractures, which means that these interfaces are not considered during evaluation. The Au precipitates were composed of 98 ± 0.3 at% Au, with ~ 1 at% Mo. One of the Mo-rich grain had a composition of 75 ± 2.2 at% Mo and 24 ± 1.9 at% C, while the other had a composition of 72 ± 3.6 at% Mo and 26 ± 3.2 at% Si. Similarly, APT revealed minimal Au atoms (< 0.5 at%) in these Mo-rich grains. While the presence of contaminants, which are discussed at the end of this section, complicates a thorough analysis, the sharp transitions and compositions between the Mo-rich grain and Au precipitate seen in the compositional profile (Fig. 6(c)) suggests phase separation of the alloy has been achieved at 800 °C. Reflections observed in the radial distribution plots (Fig. 3(d)) also display an increased intensity of Au peaks relative to the Mo peaks, further supporting that at 800 °C the microstructure is composed of phase separated bcc Mo grains and fcc Au precipitates.

In other binary nanostructured alloys, such as Fe-Cu and Cu-Co, the general observation has been that phase separation and the formation of secondary phase precipitates leads to an accelerated grain coarsening [49,56]; however, this study showed that the Mo-Au systems has maintained a sub 100 nm grain size upon annealing at 800 °C for 96 h. The retention of nanograins in the Mo-Au alloy appears to be attributed to influences from both kinetic and thermodynamic stability mechanisms. Initially, as observed at 550 °C, thermodynamic and kinetic contributions are present in the form of Au segregation zones and Au clusters, but as the temperature increased only one mechanism becomes prevalent. This switch in mechanisms is presumably facilitated by the diffusion behavior of Au, where the diffusion along GBs promotes the growth of clusters leading to the observed Au precipitates in the EDS maps (Fig. 2(c)). As a result of coarsening, the Au segregation zones are depleted of GB solute and the thermodynamic contribution is ultimately reduced. Similar behavior has been suggested in other studies, specifically after the alloys are annealed above a transition temperature where precipitation and coarsening occur [7,9]. Given that the pinning force generated by second-phase particles decreases as a function of particle size, the growth of the Au precipitates should lead to an overall reduction in kinetic stabilization [54]. The pinning pressure exerted by the precipitates (P_z) can be expressed by the Zener pinning equation, $P_z = \frac{3F_v\gamma}{2r}$, where F_{ν} refers to the volume fractions of the precipitates with radius r, and γ is the specific grain boundary energy. Thus, a combined decrease in the kinetic and thermodynamic contributions promotes the moderate grain growth observed from 550 °C to 800 °C. Furthermore, the absence of segregation zones and the presence of nanoscale Au precipitates in-

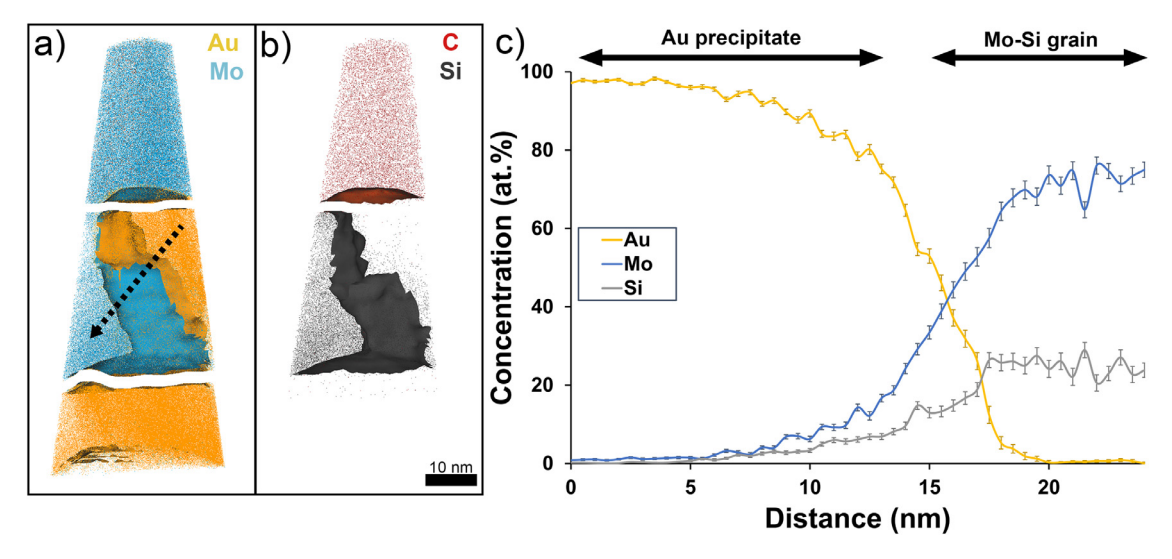


Fig. 6. APT maps from the Mo–Au sample annealed at 800 °C, where (a) shows the ion distribution of Mo (30 at% isosurface) and Au (90 at% isosurface), and (b) shows the ion distribution of C (15 at% isosurface) and Si (10 at% isosurface). Regions are separated where possible micro-fractures have occurred during APT measurements. These interfaces are not evaluated. The 1D concentration profile (c) obtained from the region indicated by the dashed arrow spans across an Au precipitate and a Mo-rich grain.

Table 1Diffusion distance (*L*) of C and Si in Mo at different temperatures with time (*t*) of 10 s.

	Temperature (°C)	D (m ^{2/s})	L (nm)
C in Mo [57]	550	1.0×10^{-16}	31
	800	1.9×10^{-14}	4.3×10^{2}
	1000	3.0×10^{-13}	1.7×10^{3}
Si in Mo [58]	550	2.6×10^{-18}	5.1
	800	3.2×10^{-13}	1.8×10^{2}
	1000	1.3×10^{-13}	1.1×10^3

dicates that the microstructure at 800 °C is predominantly stabilized by kinetic mechanisms through GB pinning.

The extent to which contaminants affect the observed microstructures is always a point of discussion since both the quantity and time of contamination can greatly alter microstructural evolution. As stated earlier, no significant contaminants were detected in samples heat-treated below 550 °C nor in similar as-sputtered samples [18,27]. However, for samples annealed at 800 °C, APT measurements revealed more than 20 at% C and Si in the Mo regions; where the most probable source of contamination results from quenching the samples above 800 °C. This assumption is based on the composition of the quenching medium, Invoil 705 (C₃₃H₃₄O₂Si₃), and the lack of contaminants in samples heattreated at lower temperatures. To further support this assumption, basic diffusion calculations for C [57] and Si [58] in Mo at select temperatures were performed (Table 1). The diffusion distances, $L \approx (Dt)^{1/2}$, were calculated for a time t = 10 s (approximation of the time required for the sample to cool in the quenching medium). From these calculations, only surface level diffusion is expected for temperatures below 550 °C; however, above 800 °C, Si and C are expected to diffuse throughout the 2 μ m thickness of the sample. These calculations agree with the APT measurements where C and Si are prominent at 800 °C, and the measured compositions suggest the formation of MoC and MoSi phases. Therefore, it is assumed that C and Si contamination occurred during quenching, which altered the final microstructural composition but should have minimal influence on the observed grain sizes and thermal stability mechanisms.

3.4. Grain growth region limit, t = 1000 °C

Upon annealing at 1000 °C, the Mo-Au system undergoes a transition from the elongated morphology seen at 800 °C to a microstructure composed of equiaxed grains, which is observed in the TEM and EDS maps in Fig. 2(d). The EDS compositional maps more clearly illustrate the Au precipitates that appear along Mo GBs, triple junctions, and within grain interiors. At 1000 °C, it is expected that the overall Au content should decrease as a consequence of the evaporation of Au at these annealing temperature and vacuum conditions. Thus, several voids are visible in the microstructure, and the number of Au precipitates has diminished in comparison to the Mo-Au microstructures observed at lower temperatures. Furthermore, as indicated by the DSC scans, grain growth is exhibited as the average grain size increased to 190 nm. Specifically, a wide size distribution for the Au precipitates is seen. Several smaller precipitates are identified within Mo grains and at triple junctions, but there are also a few Au precipitates that have reached sizes similar to the Mo grains. Note that given the overall grain size of the sample at 1000 °C, APT was not performed as TEM and EDS were considered sufficient to characterize the microstructure.

To further understand the grain growth and precipitation process at 1000 °C, EDS was performed on a Mo grain and an Au precipitate, where the respective point scans for each region of interest are shown in Fig 7. From the EDS scan, the presence of strong Au peaks and the absence of any Mo peaks indicate that the precipitates are mostly pure Au. Likewise, the EDS scan of the selected Mo rich grain shows strong Mo peaks with no identifiable Au peaks. The detected C and Si peaks in the scans can be attributed to the quenching process of these samples, as discussed in the previous section. Therefore, at these elevated temperatures, despite the pronounce changes in grain size and structure the Mo grains and Au precipitates remain phase separated with no noticeable changes in composition. These findings suggest that the observed microstructure is formed primarily through the coalescence and coarsening of the Mo grains and Au precipitates. Based on growth kinetics of nanophase immiscible systems it is expected that a bimodal growth process occurs, where the growth of Mo grains is facilitated by GB migration controlled by GB diffusion. Meanwhile, coarsening of the Au precipitates is promoted by long range volume diffusion which is similarly controlled by GB diffusion [59].

Thus, the sample annealed at $1000\,^{\circ}$ C exhibited an average grain size ~ 3 times greater than that measured at $800\,^{\circ}$ C. The increase in grain

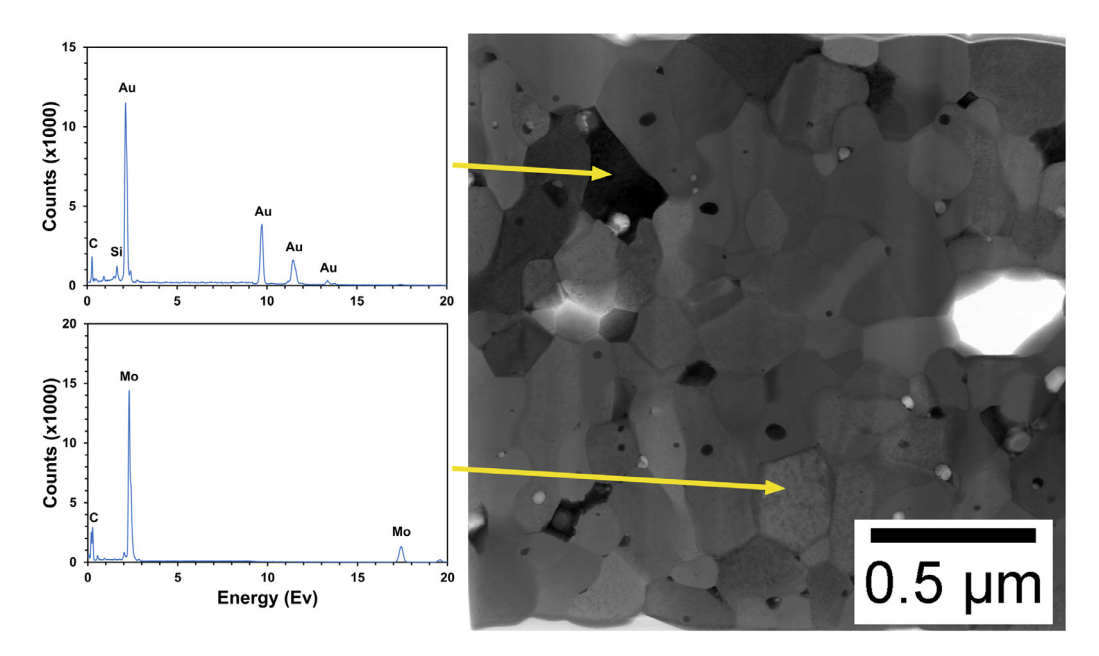


Fig. 7. EDS scans of an Au precipitate and Mo-rich grain and the corresponding cross-sectional bright field TEM image of the Mo–Au sample heat treated at 1000 °C. The red arrows indicate the respective regions where the scans were taken from.

size indicates that the drag effects produced by the Au precipitates at 800 °C have mostly been overcome at these higher temperatures. Similar to what was observed at lower temperatures, coarsening of the precipitates leads to a diminished kinetic stabilization contribution. Nevertheless, several nanometer sized Au precipitates are located at GBs, triple junctions, and within Mo grains, which are expected to generate pinning forces that resist further GB mobility [56]. Therefore, the varied coarsening behavior of the Au precipitates will generate different pinning pressures depending on the precipitate size. From the observed microstructure at 1000 °C, it does appear that kinetic stabilization mechanisms play a role since the grain size is only 190 nm.

4. Conclusions

In this study, we have investigated the microstructural evolution of an immiscible binary alloy to further understand and identify active thermal processes and stability mechanisms as a function of temperature. More specifically, complementary characterization techniques of APT and TEM were combined with DSC to explore the contributions of kinetic and thermodynamic mechanisms during the annealing stages of a Mo–Au NMMs.

Annealing the initial nanostructure to 350 °C results in a multilayer structure with roughening and intermixing between the Au and Morich layers, indicating the initial stages of degradation of the nanolaminate structure. Still, no noticeable change in grain size, 9 nm, was observed between these temperatures. Further annealing to 550 °C led to the recrystallization of the NMMs, producing a metallic nanocomposite consisting of Mo-rich grains with heterogenous Au solute behavior at the GBs. The presence of Au clusters and segregation zones along GBs indicated a coupling of kinetic and thermodynamic stabilization mechanisms which contributed to maintaining an average grain size of 37 nm. Between temperatures of 550 °C and 800 °C, the prominent thermal process is grain growth which is facilitated by phase separation of Mo grains and Au precipitates. Furthermore, the coarsening of Au precipitates through GB diffusion depletes the excess GB solute, promoting a shift to a predominantly kinetic contribution generated by precipitate pinning. At 800 °C, the Mo-Au system still retained nanoscale features, with an average grain size of 67 nm. Lastly, at 1000 °C, the Mo-Au alloy exhibits considerable grain growth leading to the formation of an equiaxed microstructure with an average grain size of 190 nm. The apparent increase in grain size indicates that the elevated temperature provides sufficient energy for the grains to overcome the drag forces generated by the Au precipitates. However, several nanometer sized Au precipitates located at GBs and within grain interiors produce an active pinning mechanism that likely mitigated further grain growth at $1000\,^{\circ}\text{C}$.

Overall, this study provides a comprehensive guide to the thermal processes and stability mechanisms responsible for the microstructural changes in Mo–Au NMMs. Annealing of the NMMs leads to the development of several complex nanostructures that were governed by recrystallization and grain growth. Furthermore, these thermal processes initiated kinetic and thermodynamic stability mechanism, which appear to be contingent on the segregation and diffusion behavior of Au atoms. Thus, the utilized methodology in combination with sputtered NMMs could be useful in identifying the active thermal processes and mechanisms that influence nanograin stability in other systems.

Declaration of interests

The authors declare that they have no known competing financial interests or personal relationships that could have appeared to influence the work reported in this paper.

The authors declare the following financial interests/personal relationships which may be considered as potential competing interests:

Acknowledgments

This work was performed under the auspices of the National Science Foundation under grants DMR-1709771 and OISE-1460006. We acknowledge D. Chassaing for FIB preparation of the APT samples and the Center for Electron Microscopy and Microanalysis at USC for the use of their SEM, FIB and TEM.

References

- [1] H. Gleiter, Nanocrystalline materials, Progress Mater. Sci. 33 (4) (1989) 223-315.
- [2] R.A. Andrievski, Review of thermal stability of nanomaterials, J. Mater. Sci. 49 (4) (2014) 1449–1460.
- 3] R.A. Andrievski, Nanostructures under extremes, Phys.-Uspekhi 57 (10) (2014) 945.
- [4] J.A. Haber, W.E. Buhro, Kinetic instability of nanocrystalline aluminum prepared by chemical synthesis; facile room-temperature grain growth, J. Am. Chem. Soc. 120 (42) (1998) 10847–10855.

- [5] A.J. Detor, C.A. Schuh, Microstructural evolution during the heat treatment of nanocrystalline alloys. J. Mater. Res. 22 (11) (2011) 3233–3248.
- [6] C.E. Krill, L. Helfen, D. Michels, H. Natter, A. Fitch, O. Masson, R. Birringer, Size-dependent grain-growth kinetics observed in nanocrystalline Fe, Phys. Rev. Lett. 86 (5) (2001) 842–845.
- [7] C.C. Koch, R.O. Scattergood, M. Saber, H. Kotan, High temperature stabilization of nanocrystalline grain size: thermodynamic versus kinetic strategies, J. Mater. Res. 28 (13) (2013) 1785–1791.
- [8] K.A. Darling, M.A. Tschopp, B.K. VanLeeuwen, M.A. Atwater, Z.K. Liu, Mitigating grain growth in binary nanocrystalline alloys through solute selection based on thermodynamic stability maps, Comput. Mater. Sci. 84 (Suppl. C) (2014) S255–S266.
- [9] K.A. Darling, A.J. Roberts, Y. Mishin, S.N. Mathaudhu, L.J. Kecskes, Grain size stabilization of nanocrystalline copper at high temperatures by alloying with tantalum, J. Alloys Compd. 573 (Suppl. C) (2013) 142–150.
- [10] T. Chookajorn, M. Park, C.A. Schuh, Duplex nanocrystalline alloys: entropic nanostructure stabilization and a case study on W-Cr, J. Mater. Res. 30 (2) (2015) 151–163.
- [11] T. Chookajorn, C.A. Schuh, Nanoscale segregation behavior and high-temperature stability of nanocrystalline W–20at% Ti, Acta Mater. 73 (2014) 128–138.
- [12] M. Kapoor, T. Kaub, K.A. Darling, B.L. Boyce, G.B. Thompson, An atom probe study on Nb solute partitioning and nanocrystalline grain stabilization in mechanically alloyed Cu–Nb, Acta Mater. 126 (Suppl. C) (2017) 564–575.
- [13] O.K. Donaldson, K. Hattar, T. Kaub, G.B. Thompson, J.R. Trelewicz, Solute stabilization of nanocrystalline tungsten against abnormal grain growth, J. Mater. Res. 33 (1) (2017) 68–80.
- [14] T. Rojhirunsakool, K.A. Darling, M.A. Tschopp, G.P. Purja Pun, Y. Mishin, R. Baner-jee, L.J. Kecskes, Structure and thermal decomposition of a nanocrystalline mechanically alloyed supersaturated Cu–Ta solid solution, MRS Commun. 5 (2) (2015) 333–339.
- [15] T. Chookajorn, H.A. Murdoch, C.A. Schuh, Design of stable nanocrystalline alloys, Science 337 (6097) (2012) 951–954.
- [16] N. Sallez, X. Boulnat, A. Borbély, J.L. Béchade, D. Fabrègue, M. Perez, Y. de Carlan, L. Hennet, C. Mocuta, D. Thiaudière, Y. Bréchet, In situ characterization of microstructural instabilities: recovery, recrystallization and abnormal growth in nanoreinforced steel powder, Acta Mater. 87 (2015) 377–389.
- [17] F. Zhou, X.Z. Liao, Y.T. Zhu, S. Dallek, E.J. Lavernia, Microstructural evolution during recovery and recrystallization of a nanocrystalline Al–Mg alloy prepared by cryogenic ball milling, Acta Mater. 51 (10) (2003) 2777–2791.
- [18] M.N. Polyakov, T. Chookajorn, M. Mecklenburg, C.A. Schuh, A.M. Hodge, Sputtered Hf-Ti nanostructures: a segregation and high-temperature stability study, Acta Mater. 108 (Suppl. C) (2016) S8–S16.
- [19] H.J. Fecht, E. Hellstern, Z. Fu, W.L. Johnson, Nanocrystalline metals prepared by high-energy ball milling, Metall. Trans. A 21 (9) (1990) 2333.
- [20] Á. Révész, T. Ungár, A. Borbély, J. Lendvai, Dislocations and grain size in ball-milled iron powder, Nanostruct. Mater. 7 (7) (1996) 779–788.
- [21] C.J. Marvel, P.R. Cantwell, M.P. Harmer, The critical influence of carbon on the thermal stability of nanocrystalline Ni–W alloys, Scr. Mater. 96 (2015) 45–48.
- [22] C.J. Marvel, D. Yin, P.R. Cantwell, M.P. Harmer, The influence of oxygen contamination on the thermal stability and hardness of nanocrystalline Ni–W alloys, Mater. Sci. Eng.: A 664 (Suppl. C) (2016) S49–S57.
- [23] M. Hecker, J. Thomas, D. Tietjen, S. Baunack, C.M. Schneider, Q. An, N. Cramer, R.E. Camley, Z. Celinski, Thermally induced modification of GMR in Co/Cu multilayers: correlation among structural, transport, and magnetic properties, J. Phys. D: Appl. Phys. 36 (5) (2003) 564.
- [24] D. Srinivasan, S. Sanyal, R. Corderman, P.R. Subramanian, Thermally stable nano-multilayer films of Cu/Mo, Metall. Mater. Trans. A 37 (3) (2006) 995–1003.
- [25] A. Misra, R.G. Hoagland, H. Kung, Thermal stability of self-supported nanolayered Cu/Nb films, Philos. Mag. 84 (10) (2004) 1021–1028.
- [26] F. Moszner, C. Cancellieri, M. Chiodi, S. Yoon, D. Ariosa, J. Janczak-Rusch, L.P.H. Jeurgens, Thermal stability of Cu/W nano-multilayers, Acta Mater. 107 (Suppl. C) (2016) S345–S353.
- [27] J.S. Riano, A.M. Hodge, Exploring the microstructural evolution of Hf-Ti: from nanometallic multilayers to nanostructures, Scr. Mater. 142 (Suppl. C) (2018) S55–S60.
- [28] H. Aboulfadl, I. Gallino, R. Busch, F. Mücklich, Atomic scale analysis of phase formation and diffusion kinetics in Ag/Al multilayer thin films, J. Appl. Phys. 120 (19) (2016) 195306.
- [29] G. Lucadamo, K. Barmak, S. Hyun, C. Cabral, C. Lavoie, Evidence of a two-stage reaction mechanism in sputter deposited Nb/Al multilayer thin-films studied by in situ synchrotron X-ray diffraction, Mater. Lett. 39 (5) (1999) 268–273.
- [30] H.A. Murdoch, C.A. Schuh, Estimation of grain boundary segregation enthalpy and its role in stable nanocrystalline alloy design, J. Mater. Res. 28 (16) (2013) 2154–2163.
- [31] H.A. Murdoch, C.A. Schuh, Stability of binary nanocrystalline alloys against grain growth and phase separation, Acta Mater. 61 (6) (2013) 2121–2132.

- [32] T.F. Kelly, D.J. Larson, Atom probe tomography 2012, Annu. Rev. Mater. Res. 42 (1) (2012) 1–31.
- [33] G.W.H. Höhne, W. Hemminger, H.J. Flammersheim, Theoretical fundamentals of differential scanning calorimeters, Differential Scanning Calorimetry, Springer, 1996, pp. 21–40.
- [34] K. Hono, D. Raabe, S.P. Ringer, D.N. Seidman, Atom probe tomography of metallic nanostructures. MRS Bull. 41 (1) (2016) 23–29.
- [35] H. Gnaser, Atom probe tomography of nanostructures, Surf. Interface Anal. 46 (2014) 383–388.
- [36] P.F. Ladwig, J.D. Olson, J.H. Bunton, D.J. Larson, R.M. Ulfig, R.L. Martens, T.T. Gribb, T.F. Kelly, M.C. Bonsager, A.E. Schultz, B.B. Pant, Y.A. Chang, Intermixing and phase separation at the atomic scale in Co-rich (Co,Fe) and Cu multilayered nanostructures, Appl. Phys. Lett. 87 (12) (2005) 121912.
- [37] K.R. Coffey, K. Barmak, A new model for grain boundary diffusion and nucleation in thin film reactions, Acta Metall. Mater. 42 (8) (1994) 2905–2911.
- [38] M. Bobeth, A. Ullrich, W. Pompe, Destratification mechanisms in coherent multilayers, J. Metastab. Nanocryst. Mater. Trans. Tech. Publ. (2004) 153.
- [39] A. Ullrich, M. Bobeth, W. Pompe, Evolution of coherent interphase boundaries during annealing of multilayers: a Monte Carlo study, Interface Sci. 12 (2) (2004) 249–257.
- [40] L. Fei, S. Lei, W.-B. Zhang, W. Lu, Z. Lin, C.H. Lam, Y. Chai, Y. Wang, Direct TEM observations of growth mechanisms of two-dimensional MoS2 flakes, Nat. Commun. 7 (2016) 12206.
- [41] K.O. Schweitz, K. Rätzke, D. Foord, P.J. Thomas, A.L. Greer, H. Geisler, J. Chevallier, J B⊘ttiger, The microstructural development of Ag/Ni multilayers during annealing, Philos. Mag. A 80 (8) (2000) 1867–1877.
- [42] R.D. Doherty, D.A. Hughes, F.J. Humphreys, J.J. Jonas, D. Juul Jensen, M.E. Kassner, W.E. King, T.R. McNelley, H.J. McQueen, A.D. Rollett, Current issues in recrystallization: a review, Mater. Today 1 (2) (1998) 14–15.
- [43] Z.R. Zeng, Y.M. Zhu, S.W. Xu, M.Z. Bian, C.H.J. Davies, N. Birbilis, J.F. Nie, Texture evolution during static recrystallization of cold-rolled magnesium alloys, Acta Mater. 105 (2016) 479–494.
- [44] J. Guyon, A. Hazotte, F. Wagner, E. Bouzy, Recrystallization of coherent nanolamellar structures in Ti48Al2Cr2Nb intermetallic alloy, Acta Mater. 103 (2016) 672–680.
- [45] A. Rollett, F.J. Humphreys, G.S. Rohrer, M. Hatherly, Recrystallization and Related Annealing Phenomena, Elsevier Science, London, 2004.
- [46] H.R. Peng, M.M. Gong, Y.Z. Chen, F. Liu, Thermal stability of nanocrystalline materials: thermodynamics and kinetics, Int. Mater. Rev. 62 (6) (2017) 303–333.
- [47] S.N. Mathaudhu, B.L. Boyce, Thermal stability: the next frontier for nanocrystalline materials, JOM 67 (12) (2015) 2785–2787.
- [48] M.R. Chellali, Z. Balogh, H. Bouchikhaoui, R. Schlesiger, P. Stender, L. Zheng, G. Schmitz, Triple junction transport and the impact of grain boundary width in nanocrystalline Cu, Nano Lett. 12 (7) (2012) 3448–3454.
- [49] B.G. Clark, K. Hattar, M.T. Marshall, T. Chookajorn, B.L. Boyce, C.A. Schuh, Thermal stability comparison of nanocrystalline Fe-based binary alloy pairs, JOM 68 (6) (2016) 1625–1633.
- [50] F. Abdeljawad, P. Lu, N. Argibay, B.G. Clark, B.L. Boyce, S.M. Foiles, Grain boundary segregation in immiscible nanocrystalline alloys, Acta Mater. 126 (Suppl. C) (2017) 5539 5530
- [51] P. Lejcek, Grain Boundary Segregation in Metals, Springer Science & Business Media, 2010.
- [52] E.J. Mittemeijer, Phase transformations, in: E.J. Mittemeijer (Ed.), Fundamentals of Materials Science: The Microstructure–Property Relationship Using Metals as Model Systems, Springer Berlin Heidelberg, Berlin, Heidelberg, 2011, pp. 371–461.
- [53] X. Zhou, X.-X. Yu, T. Kaub, R.L. Martens, G.B. Thompson, Grain boundary specific segregation in nanocrystalline Fe(Cr), Sci. Rep. 6 (2016) 34642.
- [54] R.K. Koju, K.A. Darling, L.J. Kecskes, Y. Mishin, Zener pinning of grain boundaries and structural stability of immiscible alloys, JOM 68 (6) (2016) 1596–1604.
- [55] C.J. O'Brien, C.M. Barr, P.M. Price, K. Hattar, S.M. Foiles, Grain boundary phase transformations in PtAu and relevance to thermal stabilization of bulk nanocrystalline metals, J. Mater. Sci. 53 (4) (2018) 2911–2927.
- [56] A. Bachmaier, M. Pfaff, M. Stolpe, H. Aboulfadl, C. Motz, Phase separation of a supersaturated nanocrystalline Cu–Co alloy and its influence on thermal stability, Acta Mater. 96 (2015) 269–283.
- [57] Y. Hiraoka, K. Imamura, T. Kadokura, Y. Yamamoto, Carbon diffusion behavior in molybdenum at relatively low temperatures, J. Alloys Compd. 489 (1) (2010) 42–46.
- [58] P.C. Tortorici, M.A. Dayananda, Diffusion structures in Mo vs. Si solid–solid diffusion couples, Scr. Mater. 38 (12) (1998) 1863–1869.
- [59] M. Zhu, Z.F. Wu, M.Q. Zeng, L.Z. Ouyang, Y. Gao, Bimodal growth of the nanophases in the dual-phase composites produced by mechanical alloying in immiscible Cu–Ag system, J. Mater. Sci. 43 (9) (2008) 3259–3266.